

iSLAM: Imperative SLAM

Taimeng Fu¹
taimengf@sairlab.org

Shaoshu Su¹
shaoshus@sairlab.org

Chen Wang¹
chenw@sairlab.org

¹<https://sairlab.org>

Spatial AI & Robotics (SAIR) Lab
Department of Computer Science and Engineering
State University of New York at Buffalo, United States

Abstract: Simultaneous localization and mapping (SLAM) stands as one of the critical challenges in robot navigation. Recent advancements suggest that methods based on supervised learning deliver impressive performance in front-end odometry, while traditional optimization-based methods still play a vital role in the back-end for minimizing estimation drift. In this paper, we found that such decoupled paradigm can lead to only sub-optimal performance, consequently curtailing system capabilities and generalization potential. To solve this problem, we proposed a novel self-supervised learning framework, imperative SLAM (iSLAM), which fosters reciprocal correction between the front-end and back-end, thus enhancing performance without necessitating any external supervision. Specifically, we formulate a SLAM system as a bi-level optimization problem so that the two components are bidirectionally connected. As a result, the front-end model is able to learn global geometric knowledge obtained through pose graph optimization by back-propagating the residuals from the back-end. This significantly improves the generalization ability of the entire system and thus achieves the accuracy improvement up to 45%. To the best of our knowledge, iSLAM is the first SLAM system showing that the front-end and back-end can learn jointly and mutually contribute to each other in a self-supervised manner.

Keywords: Imperative Learning, SLAM, Visual-Inertial Odometry

1 Introduction

Simultaneous localization and mapping (SLAM) is the task of tracking the trajectory of a robot as it moves through space while simultaneously building a map of the environment [1]. It is a key capability for autonomous robots to navigate and operate in unknown environments [2]. The significance and intricacies of SLAM have motivated considerable research in the field, leading to a variety of innovative solutions [3, 4, 5, 6, 7]. The design of contemporary SLAM systems generally adheres to a front-back-end architecture. In this structure, the front-end is typically responsible for interpreting sensor data and generating an initial estimate of the robot’s trajectory and the map of the environment, while the back-end refines these initial estimates to improve overall accuracy [8]. The recent technological advancements in the field have indicated that supervised learning-based methods can exhibit impressive performance in front-end odometry [9, 10, 11]. These methods utilize machine learning algorithms that require external supervision, typically in the form of a labeled dataset, to train the model, which then makes estimations without being explicitly programmed to perform the task. Meanwhile, traditional optimization-based techniques persist as an essential element for the back-end of the system, primarily responsible for minimizing estimation drift [12, 13]. These methods use geometric optimization, e.g., pose graph optimization [14], to solve SLAM problems, and often employ probability distributions and error models to reduce uncertainty and drift in the robot’s estimated path [15]. However, our work has identified an inherent limitation in this decoupled paradigm. We observed that while each component may function efficiently in isolation, the lack of an integrative approach between the two can culminate in sub-optimal performance. This decoupling subsequently impedes the system’s overall capabilities [16].

In response to this problem, we introduce a novel self-supervised learning framework, imperative SLAM (iSLAM). For the first time, this method promotes mutual correction between the front-end and back-end of a SLAM system, enhancing its overall performance without the requirement of external supervision. Specifically, this is achieved by formulating a SLAM system as a bi-level optimization problem [17], in which the network parameters are updated by high-level optimization (front-end), while the robot’s path is optimized by low-level optimization (back-end). This makes it possible to back-propagate the residuals from the back-end to the front-end model, enabling bidirectional communication between the two components. As a result, this process facilitates the front-end model to learn and incorporate global geometric knowledge derived from pose graph optimization, which is crucial for robot navigation tasks. To the best of our knowledge, iSLAM is the first SLAM system to demonstrate the potential for front-end and back-end components to learn in conjunction and reciprocally contribute to each other in a self-supervised manner. Through this work, we hope to pave the way for more robust and efficient SLAM systems that can adapt and generalize to a multitude of environments. In summary, the contribution of this work includes:

- **Framework:** We propose a novel self-supervised learning framework for SLAM, named iSLAM, which enables mutual learning between the front-end and back-end components. This cooperative symbiosis enables optimizing each other’s performance, fostering geometry knowledge learning for the front-end and improving the localization accuracy for the back-end.
- **Methodology:** We verify the new framework by designing a visual-inertial iSLAM system. Specifically, we design a differentiable scale correction module on top of a monocular VO to resolve the scale ambiguity for the front-end, and a pose-velocity graph optimization (PVGO) to fuse visual-inertial data and reduce estimation drift for the back-end.
- **Performance:** Our experiments demonstrate that by implementing the new self-learning mechanism, a typical VO network in the front-end can experience a performance enhancement of up to 45% by learning from the back-end. To benefit the broader community, we develop iSLAM as a modular system and will incorporate it into the open-source library PyPose [16].

2 Related Works

The SLAM problem has been one of the most fundamental research areas in robotics for several decades [18]. Some early works were based on probability models, utilizing filters to incrementally estimate the trajectories [19, 20, 21]. Although these methods were computationally efficient at the time, they faced issues with consistency and accuracy when tracking over longer periods. Later, the focus shifted toward factor graph optimization methods that optimize topological posterior probabilities, and they had since become the dominant approach [8]. Some works utilized Bundle Adjustment (BA) techniques to minimize the reprojection error over precalculated feature matchings [22, 3, 12] (known as indirect methods) or maximize the photometric consistency [23, 4, 24] (known as direct methods). Despite these methods demonstrated improved accuracy, they tend to demand a higher computational load. Furthermore, there has been an exploration into more lightweight pose graph optimization (PGO) techniques that focus on optimizing only the camera’s positions rather than the feature points in the back-end [14, 25]. These strategies generally incorporate loop closure techniques [26] for pose adjustments, thereby improving the reliability and accuracy of localization. Deep learning methods have witnessed significant development in recent years [6]. As data-driven approaches, they are believed to perform better on visual tracking than the engineered features [9]. Most studies on the subject employed end-to-end structures, including both supervised [27, 28, 29, 5, 30, 9] and unsupervised methods [31, 32, 33, 34, 35, 36]. It is generally observed that the supervised approaches achieve higher performance compared to their unsupervised counterparts since they can learn from a diverse range of ground truths such as pose, flow, and depth [9]. Nevertheless, obtaining such ground truth labels in real-world scenarios is a labor-consuming process [37].

Recently, hybrid methods are receiving increasing attention as they integrate the strengths of both geometry-based and deep-learning approaches. Several studies have explored the potential of integrating Bundle Adjustment (BA) with deep learning methods to impose topological consistency between frames, such as attaching a BA layer to a learning network [38, 10, 11, 39]. Additionally, some works focused on compressing image features into codes (embedded features) and optimizing

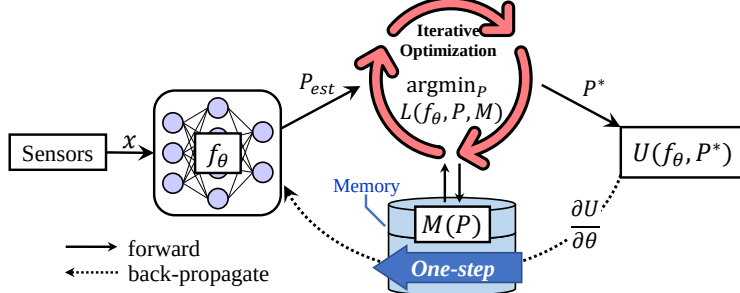


Figure 1: The framework of iSLAM, which is a bi-level optimization. On the forward path, the odometry module f_{θ} (front-end) predicts the robot trajectory and the pose graph optimization (back-end) minimizes the loss \mathcal{L} in several iterations to get optimal poses P^* . On the backward path, the loss \mathcal{U} is back-propagated through the map M with a “one-step” strategy to update the network parameters θ . This “one-step” strategy bypasses the unrolled optimization loops, leading to a more efficient and stable gradient computation.

the pose-code graph during inference [40, 41]. Furthermore, Parameshwara *et al.* [42] proposed a method that predicts poses and normal flows using networks and fine-tunes the coarse predictions through a Cheirality layer. However, in these works, the learning-based methods and geometry-based optimization are decoupled and separately used in different sub-modules. The lack of integration between the front-end and back-end may result in sub-optimal performance. In contrast, iSLAM connects them bidirectionally and enforces the learning model to learn from geometric optimization through bi-level optimization, which achieves performance improvement without external supervision. We noticed that some other tasks can also be formulated as bi-level optimization [17, 43], e.g., meta-learning [44], reinforcement learning [45], local planning [46], and combinatorial optimization [47]. To the best of our knowledge, they don’t focus on the SLAM problem and iSLAM is the first framework enabling the two components to mutually optimize each other’s performance.

3 Approach

In this section, we first introduce an overview of our iSLAM system and its bi-level optimization formulation in Section 3.1, then present the details about the front-end stereo VO, IMU pre-integration, and the back-end pose-velocity graph optimization (PVGO) in Section 3.2.1, 3.2.2, and 3.3, respectively. The training strategy of the entire framework will be presented in Section 3.4.

3.1 Overview

The framework of our iSLAM can be roughly depicted in Figure 1, which consists of three parts, i.e., an odometry network f_{θ} , a memory (map) M , and a pose graph optimization. Concretely, the entire system can be formulated as a bi-level optimization:

$$\min_{\theta} \mathcal{U}(f_{\theta}, \mathcal{L}^*), \quad (1a)$$

$$\text{s. t. } P^* = \arg \min_P \mathcal{L}(f_{\theta}, P, M), \quad (1b)$$

where P is the robot’s poses to be optimized and \mathcal{U} and \mathcal{L} are the high-level and low-level objective functions, respectively. P^* is the optimal pose in the low-level optimization, while \mathcal{L}^* is the optimal low-level objective, i.e., $\mathcal{L}(f_{\theta}, P^*, M)$. In this work, both \mathcal{U} and \mathcal{L} are geometry-based objective functions such as the pose transform residuals in PVGO. Thus the entire framework is label-free, resulting in a self-supervised approach. Intuitively, to have a lower loss, the odometry network will be driven to generate outputs that align with the geometrical reality, imposed by the geometry-based objectives. The acquired geometrical information is stored in the network parameter θ and map M for future reference and to contribute to a more comprehensive understanding of the environment. This framework is named “imperative SLAM” to emphasize the passive nature of this process.

3.2 Front-end Odometry

As depicted in Figure 2, we developed a visual-inertial odometry network, which serves as the front-end of iSLAM. It comprises a learning-based stereo visual odometry (VO) and an IMU pre-integrator. The stereo VO module takes consecutive stereo images $\{I_k^L, I_k^R, I_{k+1}^L\}$ as input, where

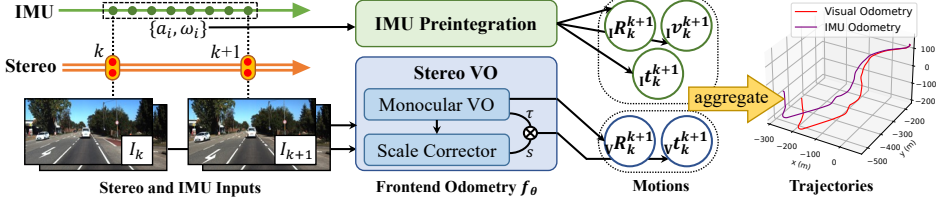


Figure 2: An overview of the front-end odometry in iSLAM. It comprises a learning-based stereo VO and an IMU pre-integrator. The two odometry modules estimate the robot’s motion, which is then aggregated and transmitted to the back-end for optimization.

k is the frame index. It estimates the relative camera motion $v\delta_k^{k+1}$ from frame k to $k+1$. The left subscript “V” indicates the result is from VO. We apply the same naming convention to other notations throughout the paper. The IMU pre-integrator takes synchronized IMU accelerations $\{a_i\}$ and gyro data $\{\omega_i\}$ to integrate the relative rotation ${}_1R_k^{k+1}$, velocity ${}_1v_k^{k+1}$, and translation ${}_1t_k^{k+1}$.

3.2.1 Learning-based Stereo Visual Odometry

During experiments, it was observed that current state-of-the-art learning-based visual odometry (VO) methods primarily concentrate on monocular settings [9], which are prone to the scale ambiguity problem arising from epipolar geometry theory [48]. On the other hand, the overall performance of stereo VO models, which can estimate the scale, remains unsatisfactory [34, 31]. We speculate that this shortcoming might arise from a network’s limited ability to concurrently predict rotation and absolute translation. To address this challenge, we propose a two-step approach: we first develop a monocular VO network to predict rotation and the direction of translation, and then utilize the stereo pair to estimate the scale factor by leveraging a fast closed-form solution.

Specifically, the scale estimation is formulated into a least squares problem over reprojection errors $\mathcal{E}^{u,v}$, where u, v are image coordinates. We first employ a disparity network [49] and an optical flow network [50] to estimate dense disparity (inverse depth) and flow map, respectively. Then we use the estimated depth and flow to calculate \mathcal{E} , and finally optimize the scale s to minimize it:

$$s^* = \arg \min_s \sum_{u,v \in I} \|\mathcal{E}^{u,v}\|_2^2, \quad (2)$$

Detailed formula derivation is presented in Appendix A. In experiments, we observed that textureless areas tend to introduce errors in depth and flow estimation. To mitigate this issue, we employ the Canny edge detector [51] to generate a mask that selectively preserves regions near edges. This approach aids in masking out blurry regions caused by factors like out-of-focus or motion blur and also eliminates areas lacking textures. Additionally, we employ a threshold filter on the disparity maps to exclude the sky and distant objects. This ensures that only feature-rich regions in close proximity to the robot are considered, enhancing the reliability and accuracy of the scale calculation.

3.2.2 Differentiable IMU Pre-integration

We follow the differentiable IMU pre-integration algorithm in PyPose [16] to implement this module. Suppose there are m IMU frames between camera frames k and $k+1$, and let $\{a_i \mid i = 1 \dots m\}$ represent accelerations, $\{\omega_i \mid i = 1 \dots m\}$ represents gyro measurements, and $\{\Delta_{i+1}^i \mid i = 1 \dots m-1\}$ represents time between adjacent IMU frames. The pre-integration is formulated by $\delta R_{i+1} = \delta R_i \cdot \text{Exp}(\omega_i \cdot \Delta_{i+1}^i)$; $\delta v_{i+1} = \delta v_i + \delta R_i \cdot a_i \cdot \Delta_{i+1}^i$; $\delta t_{i+1} = \delta t_i + \delta v_i \cdot \Delta_{i+1}^i + \frac{1}{2} \delta R_i \cdot a_i (\Delta_{i+1}^i)^2$, with initial status $\delta R_1 = I$, $\delta v_1 = 0$, and $\delta t_1 = 0$. Finally, it outputs ${}_1R_k^{k+1} = \delta R_m$, ${}_1v_k^{k+1} = \delta v_m$, and ${}_1t_k^{k+1} = \delta t_m$ as the IMU pre-integration result from camera frame k to $k+1$.

3.3 Back-end Pose-velocity Graph Optimization

In iSLAM, the pose-velocity graph plays a crucial role as it integrates the estimates from visual odometry and inertial odometry. The two data sources with different error distributions can verify and correct each other through constraints in the graph, thereby contributing to a more accurate trajectory through optimization. To match the objective, we put poses and velocities of N frames at graph nodes and make them decision variables of the optimization problem. We design four constraints to connect these nodes based on the estimations from VO and IMU. Figure 3 illustrates

the pose-velocity graph structure. The symbols $P_k = [R_k \ t_k]$ represent pose nodes, while v_k corresponds to velocity nodes. Next, we introduce the four edge constraints in the graph.

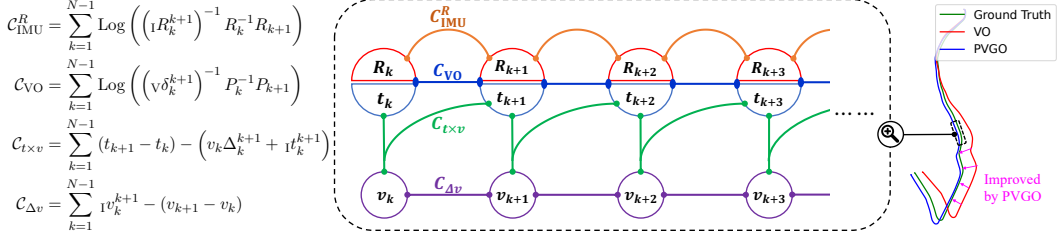


Figure 3: The pose-velocity graph structure. The nodes are poses R_k, t_k and velocities v_k , while the edges are four types of constraints. By optimizing the graph nodes via edge connections, we improve the trajectory, as shown on the right. The ground truth is only for visualization, not used in the graph optimization.

IMU Rotational Constraint The $\mathcal{C}_{\text{IMU}}^R$ introduces the IMU rotations. It measures the disagreement between graph delta rotation $R_k^{-1} R_{k+1}$ and IMU delta rotation ${}_1 R_k^{k+1}$ in Lie algebra \mathfrak{so}_3 .

VO Estimation Constraint The \mathcal{C}_{VO} links the poses with the relative camera motions estimated by the stereo VO. It measures the inconsistency between the calculated motion in graph $P_k^{-1} P_{k+1}$ and the corresponding VO motion estimation $v \delta_k^{k+1}$ in Lie algebra \mathfrak{se}_3 . $\text{Log}(\cdot)$ is the Log-mapping.

Translation-velocity Cross Constraint The $\mathcal{C}_{t \times v}$ is the bridge between positions and velocities. It measures the difference of position displacement in graph $t^{k+1} - t_k$ and the integration of graph velocity v_k over delta time Δ_k^{k+1} plus zero-initial-speed IMU acceleration integration ${}_1 t_k^{k+1}$.

Delta Velocity Constraint The $\mathcal{C}_{\Delta v}$ links the velocities with the IMU pre-integration results. It measures the difference between the delta velocity in graph $v_{k+1} - v_k$ and IMU delta velocity ${}_1 v_k^{k+1}$. The translation-velocity cross constraint makes the positions and velocities interfere with each other and sew the graph as a whole. During optimization, the IMU delta velocity constraint propagates through it to improve the pose accuracy, while the VO estimation constraint propagates through it to eliminate the IMU drift. Pose-velocity graph optimization is the low-level optimization in (1). The objective function is defined as the weighted sum of the four constraint losses,

$$\mathcal{L} = w_1 \mathcal{C}_{\text{VO}} + w_2 \mathcal{C}_{\Delta v} + w_3 \mathcal{C}_{\text{IMU}}^R + w_4 \mathcal{C}_{t \times v}, \quad (3)$$

where w_1-w_4 are weights. We employ the Levenberg-Marquardt (LM) optimizer in PyPose [16] to perform the pose graph optimization, which is a popular method for solving nonlinear least squares problems. The optimal poses R_k^*, t_k^* are transmitted to and stored in map M for future reference.

3.4 The One-step Back-propagation Strategy

In this section, we present the optimization process described in (1). This process aims to back-propagate the high-level objective \mathcal{U} to the front-end odometry to achieve self-supervised imperative learning. However, the challenge lies in the fact that the LM optimizer used in low-level optimization typically requires multiple iterations to converge, leading to complicated gradient computation. The strategy of back-propagating through unrolling the iterative forward path, as used in [38, 10], is inefficient and also error-prone due to numerical instabilities. In contrast, we apply an efficient “one-step” strategy that utilizes the nature of stationary points to solve this problem. According to the chain rule, we can calculate the gradient of \mathcal{U} with respect to the front-end model parameters θ

$$\frac{\partial \mathcal{U}}{\partial \theta} = \frac{\partial \mathcal{U}}{\partial f_\theta} \frac{\partial f_\theta}{\partial \theta} + \frac{\partial \mathcal{U}}{\partial \mathcal{L}^*} \left(\frac{\partial \mathcal{L}^*}{\partial f_\theta} \frac{\partial f_\theta}{\partial \theta} + \frac{\partial \mathcal{L}^*}{\partial P^*} \frac{\partial P^*}{\partial \theta} \right). \quad (4)$$

Intuitively, the partial derivative term $\frac{\partial P^*}{\partial \theta}$ embeds the gradients from the iterative optimization, which is very computationally heavy. However, if we assume the low-level optimization converges to the optimal (either global or local), we have a stationary point $\frac{\partial \mathcal{L}^*}{\partial P^*} \approx 0$, which eliminates the complex gradient term $\frac{\partial P^*}{\partial \theta}$ and bypasses the low-level optimization iterations. The choice of \mathcal{U} is case-specific and it can be back-propagated in one step as long as it incorporates \mathcal{L} as the sole term involving P^* . Here we select \mathcal{U} to be identical to \mathcal{L} for simplicity, although they’re not necessarily the same in general cases. In practice, as only the VO module in the front-end is learnable, \mathcal{U} can be further simplified as \mathcal{C}_{VO} . We also assign different weights to its rotational and translational

Table 1: The RMSE drifts on KITTI for VO methods. Specifically, r_{rel} is rotational RMSE drift ($^{\circ}/100$ m), t_{rel} is translational RMSE drift (%) on a length of 100–800 m, and “–” denotes the data is not available.

	Methods	Supervision	00	01	02	04	05	06	07	08	09	10	Avg
r_{rel}	DeepVO [5]	✓	-	-	-	6.970	3.610	5.820	4.600	-	-	8.830	5.966
	Zhan <i>et al.</i> [34]	✗	-	-	-	-	-	-	-	-	3.600	3.430	-
	UnDeepVO [31]	✗	1.920	-	2.440	-	1.500	1.980	2.480	1.790	-	4.650	2.394
	TartanVO [9]	✓	3.695	1.938	3.433	4.371	3.150	2.262	4.545	3.109	2.994	2.802	3.230
	Ours (VO only)	✗	2.647	1.198	1.869	0.663	1.483	1.162	1.753	1.810	1.409	1.399	1.539
t_{rel}	DeepVO [5]	✓	-	-	-	7.190	2.620	5.420	3.910	-	-	8.110	5.450
	Zhan <i>et al.</i> [34]	✗	-	-	-	-	-	-	-	-	11.930	12.450	-
	UnDeepVO [31]	✗	4.140	-	5.580	-	3.400	6.200	3.150	4.080	-	10.630	5.311
	TartanVO [9]	✓	6.396	6.466	4.854	6.459	5.896	4.226	7.914	6.490	7.221	9.100	6.502
	Ours (VO only)	✗	5.304	6.425	4.686	7.152	3.656	4.399	3.228	4.344	4.220	4.633	4.805

Table 2: The rotational and translational RMSE drifts on KITTI for VIO methods.

	Methods	Supervision	00	01	02	04	05	06	07	08	09	10	Avg
r_{rel}	Wei <i>et al.</i> [52]	✗	0.960	0.610	0.590	0.490	0.730	0.920	0.830	0.670	0.890	0.530	0.722
	Yang <i>et al.</i> [53]	✓	-	-	-	-	0.750	-	0.760	-	-	1.080	-
	DeepVIO [54]	✗	2.450	-	1.440	2.320	-	-	1.660	1.020	1.120	1.030	1.577
	Ours	✗	2.156	0.120	0.593	0.067	0.374	0.193	0.270	0.271	0.230	0.208	0.448
	Wei <i>et al.</i> [52]	✗	3.670	16.700	3.110	1.950	3.320	4.480	3.490	4.740	4.130	5.510	5.110
t_{rel}	Yang <i>et al.</i> [53]	✓	-	-	-	-	2.010	-	1.790	-	-	3.410	-
	DeepVIO [54]	✗	11.620	-	4.520	-	2.860	-	2.710	2.130	1.380	0.850	3.724
	Ours	✗	6.366	6.700	2.850	6.280	1.947	3.161	2.152	2.761	2.434	2.069	3.672

components to balance their impacts and stabilize the training.

$$\mathcal{U} = w_r \sum_{k=1}^{N-1} \text{Log} \left(\left(\mathbf{v} R_k^{k+1} \right)^{-1} R_k^{*-1} R_{k+1}^* \right) + w_t \sum_{k=1}^{N-1} \mathbf{v} t_k^{k+1} - R_k^{*-1} (t_{k+1}^* - t_k^*), \quad (5)$$

where R_k^* , t_k^* are optimal rotations and translations obtained from the map M ; w_r , w_t are weights.

4 Experimental Results

4.1 Implementation, Datasets, and Evaluation Metrics

The experimental evaluation is conducted on two widely-used benchmark datasets, namely KITTI [55] and EuRoC [56]. Both datasets comprise stereo images and IMU data; however, their motion patterns differ greatly. KITTI, as a dataset geared toward autonomous driving, includes high-speed long-range motions but very few movements on the vertical axis. On the other hand, EuRoC contains more aggressive motions in all directions but is limited to an indoor space. The diversity of motion patterns allows for demonstrating the generalization capability of iSLAM. Following prior works, we choose Absolute Trajectory Error (ATE) [57] to evaluate the trajectory accuracy, and Root Mean Square Error (RMSE) to evaluate the rotational and translational drifts.

For the front-end, we adopt the structure of TartanVO [9] as the monocular part in our VO module. It's worth noticing that the model is trained on TartanAir [37] and has never seen KITTI or EuRoC, thus the performance will be able to demonstrate the generalization ability of the proposed self-supervised learning framework. In the back-end, Cholesky is selected as the linear solver in the LM optimizer, and a TrustRegion strategy is used to change the damping rate adaptively. The model is updated using Adam optimizer with a batch size of 8 and a learning rate of 3e-6.

4.2 Accuracy Evaluation

KITTI The KITTI benchmark has been widely used in previous works across various settings and configurations. To facilitate a fair and comprehensive comparison, we evaluate our VO module against other state-of-the-art (SOTA) VO modules in Table 1 and compare the full iSLAM system to other VIO modules in Table 2. The IMU data is unavailable in sequence 03 and thus is not included.

Our method, in both the VO-only and full iSLAM settings, outperforms other SOTA competitors. Notably, the VO-only setting exhibits 74% less rotational error and 12% less translational error than DeepVO [5] (Table 1), while the full iSLAM achieves 67% less rotational error and 14% less translational error than Yang *et al.* [53] on sequences they tested on (Table 2). Notably, both DeepVO and Yang *et al.* [53] were trained with ground truth labels, while ours was self-supervised.

Table 3: EuRoC Absolute Trajectory Errors (ATE).

Methods	MH01	MH02	MH03	MH04	MH05	V101	V102	V103	V201	V202	V203	Avg
DeepV2D [58]	0.739	1.144	0.752	1.492	1.567	0.981	0.801	1.570	0.290	2.202	2.743	1.354
DeepFactors [41]	1.587	1.479	3.139	5.331	4.002	1.520	0.679	0.900	0.876	1.905	1.021	2.085
TartanVO [9]	0.783	0.415	0.778	1.502	1.164	0.527	0.669	0.955	0.523	0.899	1.257	0.869
Ours (VO Only)	<u>0.516</u>	<u>0.399</u>	<u>0.682</u>	<u>1.376</u>	<u>1.153</u>	<u>0.531</u>	<u>0.427</u>	<u>0.407</u>	<u>0.433</u>	<u>0.605</u>	<u>1.217</u>	<u>0.659</u>
Ours	0.500	0.391	0.656	1.285	1.088	0.521	0.405	0.397	0.421	0.580	1.180	0.613

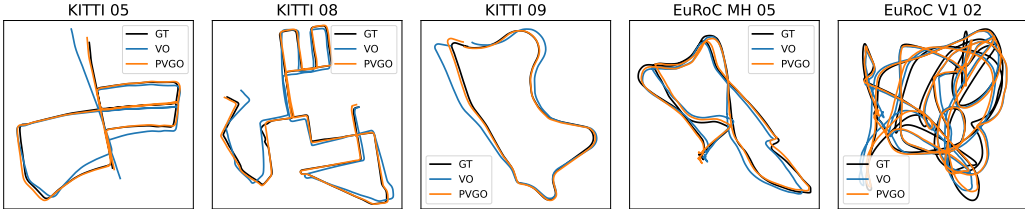


Figure 4: Estimated trajectories by our VO and PVGO on KITTI and EuRoC datasets. GT: Ground Truth, VO: visual odometry, PVGO: pose-velocity graph optimization.

EuRoC The EuRoC benchmark is captured by a micro aerial vehicle with sensors onboard. The dataset poses a significant challenge to SLAM algorithms as it features aggressive motion, large IMU drift, and significant illumination changes [13]. However, both our stereo VO and the full iSLAM generalize well to EuRoC. As shown in Table 3, iSLAM achieves an average ATE 55% lower than DeepV2D [58], 71% lower than DeepFactors [41], and 29% lower than TartanVO [9].

Qualitative analysis Several trajectories produced by iSLAM are visualized in Figure 4. It is seen that the trajectories after PVGO are in close proximity to the ground truth (GT), while the VO trajectories only exhibit minimum drift.

4.3 Effectiveness Validation

This section presents an effectiveness validation of imperative learning for enhancing system accuracy in a self-supervised manner. To demonstrate the generalizability of the proposed training strategy to any learning-based front-end, we evaluate with both our stereo VO and TartanVO [9] as the front-end VO model. Since TartanVO is a monocular VO that suffers scale ambiguity, we recover its scale estimation externally through ground truth.

The decrease in average ATE throughout imperative iterations is illustrated in Figure 5. It is observed that on both kinds of front-ends, the imperative supervision reduces the ATE by 25%-45% and 15%-20% on KITTI and EuRoC benchmarks, respectively, within six iterations. This shows that the front-end VO network has successfully learned from the back-end geometry-based optimization through the bi-level optimization, achieving performance improvement without referring to the ground truth. Besides, the performance gain in VO also improves the PVGO result, achieving approximately 15% lower ATE on both benchmarks. The result strongly supports our claim about mutual learning between the front-end and back-end. The improvement of stereo VO is visualized in Figure 6, which shows that the VO trajectories are adjusted towards the ground truth through imperative learning.

4.4 Partial Back-propagation Generalization Test

In practice, the front-end and back-end of a SLAM system often run on different processes or devices, connected through memory buffers or networks. This may lead to communication bottlenecks

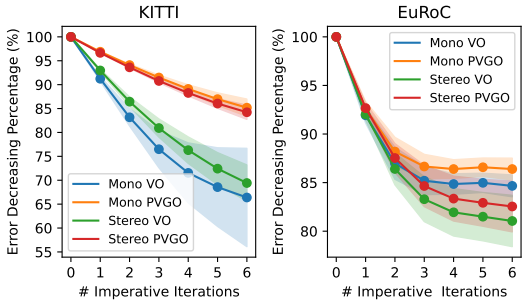


Figure 5: Percentage of the ATE decrease with respect to the number of imperative iterations. The solid line represents the average decrease rate of the ATE across all trajectories, and the transparent regions in the same color indicate their variance.

Table 4: The VO Improvement with Partial Residual Back-propagation.

		KITTI						EoRoC		
		r_{rel}			t_{rel}			ATE	50%	100%
		25%	50%	100%	25%	50%	100%	25%	50%	100%
Stereo	Before	3.224			7.458			0.808		
	After	1.633	1.647	1.539	5.051	4.966	4.805	0.666	0.659	0.659
	Improved (%)	49.35	48.90	52.25	32.28	33.42	35.58	17.47	18.44	18.44
Mono	Before	3.226			6.841			0.689		
	After	1.592	1.611	1.561	4.413	4.551	4.502	0.573	0.569	0.573
	Improved (%)	50.67	50.06	51.61	35.49	33.47	34.19	16.96	17.54	16.96

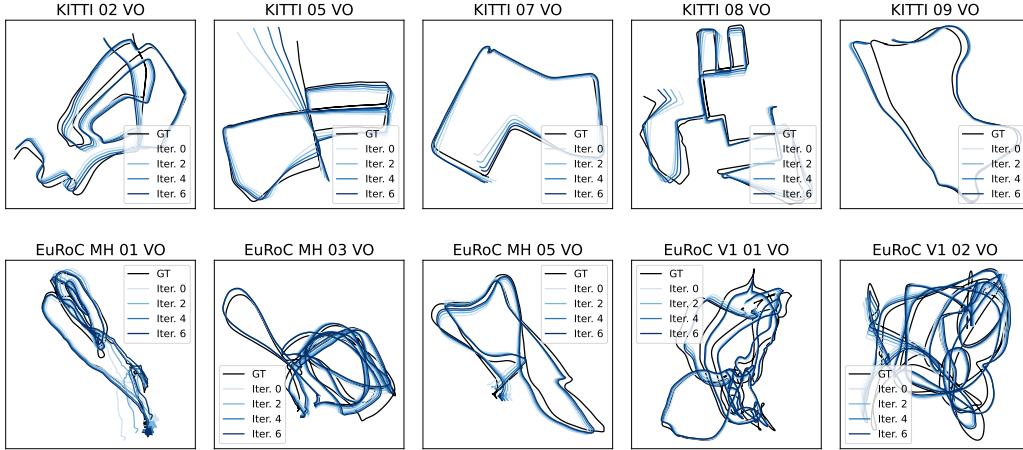


Figure 6: Comparison of trajectory estimated by our VO at different iterations of imperative learning (0, 2, 4, and 6) alongside the ground truth trajectories from KITTI and EuRoC datasets.

between the two modules. In order to explore the performance of imperative learning under such constraints, we conduct experiments involving partially back-propagate the pose transform residuals \mathcal{U} in a sequence, simulating insufficient bandwidth. The results summarized in Table 4 show the VO performance in scenarios where 25%, 50%, and 100% of error terms in \mathcal{U} are back-propagated. It is seen that all these settings result in a substantial improvement in VO model accuracy: around 50% improvement in rotation and 34% improvement in translation are observed on KITTI and around 17% ATE improvement is observed on EuRoC. The percentage of ATE improvement remains almost the same as fewer error terms are back-propagated, which indicates that the proposed iSLAM framework is highly effective even when partially applied to a sequence, thereby demonstrating its practicality for use in distributed systems with large front-back-end communication limitations.

5 Limitations & Conclusion

Despite the success of iSLAM in front-back-end collaboration, it has some limitations. First, we used a relatively simple IMU model that does not participate in the learning process. It's possible to incorporate an advanced IMU model with learnable bias and covariance and tune its parameters with a similar imperative learning paradigm. Additionally, it's also possible to perform learning-based loop closure in PVGO and apply imperative learning. In summary, the potential of the proposed imperative learning paradigm is vast, and we only provided a limited example in this paper. We hope our work will inspire more researchers to explore these exciting research directions.

To summarize, we presented iSLAM, a novel visual-inertial SLAM system that leverages imperative learning to enable its front-end and back-end to mutually learn and contribute to the overall accuracy. We formulated the imperative learning process as a bi-level optimization problem and designed a system with a stereo VO, an IMU pre-integrator, and a PVGO module to demonstrate its effectiveness. A one-step back-propagation strategy is used for efficiency. Experiments showed that iSLAM exhibits state-of-the-art accuracy on KITTI and EuRoC datasets, and achieved up to 45% performance improvements on the VO network through self-supervised imperative learning.

Acknowledgments

This work was partially supported by Cisco Systems, Inc.

References

- [1] T. Taketomi, H. Uchiyama, and S. Ikeda. Visual slam algorithms: A survey from 2010 to 2016. *IPSJ Transactions on Computer Vision and Applications*, 9(1):1–11, 2017.
- [2] K. Yousif, A. Bab-Hadiashar, and R. Hoseinnezhad. An overview to visual odometry and visual slam: Applications to mobile robotics. *Intelligent Industrial Systems*, 1(4):289–311, 2015.
- [3] R. Mur-Artal, J. M. M. Montiel, and J. D. Tardos. Orb-slam: a versatile and accurate monocular slam system. *IEEE transactions on robotics*, 31(5):1147–1163, 2015.
- [4] J. Engel, V. Koltun, and D. Cremers. Direct sparse odometry. *IEEE transactions on pattern analysis and machine intelligence*, 40(3):611–625, 2017.
- [5] S. Wang, R. Clark, H. Wen, and N. Trigoni. Deepvo: Towards end-to-end visual odometry with deep recurrent convolutional neural networks. In *2017 IEEE international conference on robotics and automation (ICRA)*, pages 2043–2050. IEEE, 2017.
- [6] S. Zhao, P. Wang, H. Zhang, Z. Fang, and S. Scherer. Tp-tio: A robust thermal-inertial odometry with deep thermalpoint. In *2020 IEEE/RSJ International Conference on Intelligent Robots and Systems (IROS)*, pages 4505–4512. IEEE, 2020.
- [7] K. Xu, Y. Hao, C. Wang, and L. Xie. Airvo: An illumination-robust point-line visual odometry. *arXiv preprint arXiv:2212.07595*, 2022.
- [8] C. Cadena, L. Carlone, H. Carrillo, Y. Latif, D. Scaramuzza, J. Neira, I. Reid, and J. J. Leonard. Past, present, and future of simultaneous localization and mapping: Toward the robust-perception age. *IEEE Transactions on robotics*, 32(6):1309–1332, 2016.
- [9] W. Wang, Y. Hu, and S. Scherer. Tartanvo: A generalizable learning-based vo. In *Conference on Robot Learning*, pages 1761–1772. PMLR, 2021.
- [10] Z. Teed and J. Deng. Droid-slam: Deep visual slam for monocular, stereo, and rgbd cameras. *Advances in neural information processing systems*, 34:16558–16569, 2021.
- [11] Z. Teed, L. Lipson, and J. Deng. Deep patch visual odometry. *arXiv preprint arXiv:2208.04726*, 2022.
- [12] C. Campos, R. Elvira, J. J. G. Rodríguez, J. M. Montiel, and J. D. Tardós. Orb-slam3: An accurate open-source library for visual, visual–inertial, and multimap slam. *IEEE Transactions on Robotics*, 37(6):1874–1890, 2021.
- [13] T. Qin, P. Li, and S. Shen. Vins-mono: A robust and versatile monocular visual-inertial state estimator. *IEEE Transactions on Robotics*, 34(4):1004–1020, 2018.
- [14] M. Labbe and F. Michaud. Online global loop closure detection for large-scale multi-session graph-based slam. In *2014 IEEE/RSJ International Conference on Intelligent Robots and Systems*, pages 2661–2666. IEEE, 2014.
- [15] J. A. Placed, J. Strader, H. Carrillo, N. Atanasov, V. Indelman, L. Carlone, and J. A. Castellanos. A survey on active simultaneous localization and mapping: State of the art and new frontiers. *IEEE Transactions on Robotics*, 2023.
- [16] C. Wang, D. Gao, K. Xu, J. Geng, Y. Hu, Y. Qiu, B. Li, F. Yang, B. Moon, A. Pandey, Aryan, J. Xu, T. Wu, H. He, D. Huang, Z. Ren, S. Zhao, T. Fu, P. Reddy, X. Lin, W. Wang, J. Shi, R. Talak, K. Cao, Y. Du, H. Wang, H. Yu, S. Wang, S. Chen, A. Kashyap, R. Bandaru, K. Dantu, J. Wu, L. Xie, L. Carlone, M. Hutter, and S. Scherer. PyPose: A library for robot learning with physics-based optimization. In *IEEE/CVF Conference on Computer Vision and Pattern Recognition (CVPR)*, 2023.
- [17] R. Liu, J. Gao, J. Zhang, D. Meng, and Z. Lin. Investigating bi-level optimization for learning and vision from a unified perspective: A survey and beyond. *IEEE Transactions on Pattern Analysis and Machine Intelligence*, 44(12):10045–10067, 2021.
- [18] J. Aulinas, Y. Petillot, J. Salvi, and X. Lladó. The slam problem: a survey. *Artificial Intelligence Research and Development*, pages 363–371, 2008.

[19] A. J. Davison, I. D. Reid, N. D. Molton, and O. Stasse. Monoslam: Real-time single camera slam. *IEEE transactions on pattern analysis and machine intelligence*, 29(6):1052–1067, 2007.

[20] M. Montemerlo, S. Thrun, D. Koller, B. Wegbreit, et al. Fastslam: A factored solution to the simultaneous localization and mapping problem. *Aaai/iaai*, 593598, 2002.

[21] A. I. Mourikis and S. I. Roumeliotis. A multi-state constraint kalman filter for vision-aided inertial navigation. In *Proceedings 2007 IEEE international conference on robotics and automation*, pages 3565–3572. IEEE, 2007.

[22] G. Klein and D. Murray. Parallel tracking and mapping for small ar workspaces. In *2007 6th IEEE and ACM international symposium on mixed and augmented reality*, pages 225–234. IEEE, 2007.

[23] J. Engel, T. Schöps, and D. Cremers. Lsd-slam: Large-scale direct monocular slam. In *Computer Vision–ECCV 2014: 13th European Conference, Zurich, Switzerland, September 6–12, 2014, Proceedings, Part II 13*, pages 834–849. Springer, 2014.

[24] C. Forster, M. Pizzoli, and D. Scaramuzza. Svo: Fast semi-direct monocular visual odometry. In *2014 IEEE international conference on robotics and automation (ICRA)*, pages 15–22. IEEE, 2014.

[25] N. Sünderhauf and P. Protzel. Towards a robust back-end for pose graph slam. In *2012 IEEE international conference on robotics and automation*, pages 1254–1261. IEEE, 2012.

[26] D. Gao, C. Wang, and S. Scherer. Airloop: Lifelong loop closure detection. In *2022 International Conference on Robotics and Automation (ICRA)*, pages 10664–10671. IEEE, 2022.

[27] G. Costante, M. Mancini, P. Valigi, and T. A. Ciarfuglia. Exploring representation learning with cnns for frame-to-frame ego-motion estimation. *IEEE robotics and automation letters*, 1(1):18–25, 2015.

[28] Z. Laskar, I. Melekhov, S. Kalia, and J. Kannala. Camera relocalization by computing pairwise relative poses using convolutional neural network. In *Proceedings of the IEEE International Conference on Computer Vision Workshops*, pages 929–938, 2017.

[29] B. Ummenhofer, H. Zhou, J. Uhrig, N. Mayer, E. Ilg, A. Dosovitskiy, and T. Brox. Demon: Depth and motion network for learning monocular stereo. In *Proceedings of the IEEE conference on computer vision and pattern recognition*, pages 5038–5047, 2017.

[30] X. Wang, D. Maturana, S. Yang, W. Wang, Q. Chen, and S. Scherer. Improving learning-based ego-motion estimation with homomorphism-based losses and drift correction. In *2019 IEEE/RSJ International Conference on Intelligent Robots and Systems (IROS)*, pages 970–976. IEEE, 2019.

[31] R. Li, S. Wang, Z. Long, and D. Gu. Undeepvo: Monocular visual odometry through unsupervised deep learning. In *2018 IEEE international conference on robotics and automation (ICRA)*, pages 7286–7291. IEEE, 2018.

[32] A. Ranjan, V. Jampani, L. Balles, K. Kim, D. Sun, J. Wulff, and M. J. Black. Competitive collaboration: Joint unsupervised learning of depth, camera motion, optical flow and motion segmentation. In *Proceedings of the IEEE/CVF conference on computer vision and pattern recognition*, pages 12240–12249, 2019.

[33] Z. Yin and J. Shi. Geonet: Unsupervised learning of dense depth, optical flow and camera pose. In *Proceedings of the IEEE conference on computer vision and pattern recognition*, pages 1983–1992, 2018.

[34] H. Zhan, R. Garg, C. S. Weerasekera, K. Li, H. Agarwal, and I. Reid. Unsupervised learning of monocular depth estimation and visual odometry with deep feature reconstruction. In *Proceedings of the IEEE conference on computer vision and pattern recognition*, pages 340–349, 2018.

[35] T. Zhou, M. Brown, N. Snavely, and D. G. Lowe. Unsupervised learning of depth and ego-motion from video. In *Proceedings of the IEEE conference on computer vision and pattern recognition*, pages 1851–1858, 2017.

[36] L. Zhou and M. Kaess. Windowed bundle adjustment framework for unsupervised learning of monocular depth estimation with u-net extension and clip loss. *IEEE Robotics and Automation Letters*, 5(2):3283–3290, 2020.

[37] W. Wang, D. Zhu, X. Wang, Y. Hu, Y. Qiu, C. Wang, Y. Hu, A. Kapoor, and S. Scherer. Tartanair: A dataset to push the limits of visual slam. In *2020 IEEE/RSJ International Conference on Intelligent Robots and Systems (IROS)*, pages 4909–4916. IEEE, 2020.

[38] C. Tang and P. Tan. Ba-net: Dense bundle adjustment network. *arXiv preprint arXiv:1806.04807*, 2018.

[39] Y.-J. Cao, X.-S. Zhang, F.-Y. Luo, P. Peng, C. Lin, K.-F. Yang, and Y.-J. Li. Learning generalized visual odometry using position-aware optical flow and geometric bundle adjustment. *Pattern Recognition*, 136:109262, 2023.

[40] M. Bloesch, J. Czarnowski, R. Clark, S. Leutenegger, and A. J. Davison. Codeslam—learning a compact, optimisable representation for dense visual slam. In *Proceedings of the IEEE conference on computer vision and pattern recognition*, pages 2560–2568, 2018.

[41] J. Czarnowski, T. Laidlow, R. Clark, and A. J. Davison. Deepfactors: Real-time probabilistic dense monocular slam. *IEEE Robotics and Automation Letters*, 5(2):721–728, 2020.

[42] C. M. Parameshwara, G. Hari, C. Fermüller, N. J. Sanket, and Y. Aloimonos. Diffposenet: Direct differentiable camera pose estimation. In *Proceedings of the IEEE/CVF Conference on Computer Vision and Pattern Recognition*, pages 6845–6854, 2022.

[43] S. Gould, R. Hartley, and D. Campbell. Deep declarative networks. *IEEE Transactions on Pattern Analysis and Machine Intelligence*, 44(8):3988–4004, 2021.

[44] L. Franceschi, M. Donini, P. Frasconi, and M. Pontil. A bridge between hyperparameter optimization and learning-to-learn. *arXiv preprint arXiv:1712.06283*, 2017.

[45] M. Hong, H.-T. Wai, Z. Wang, and Z. Yang. A two-timescale framework for bilevel optimization: Complexity analysis and application to actor-critic. *arXiv preprint arXiv:2007.05170*, 2020.

[46] F. Yang, C. Wang, C. Cadena, and M. Hutter. iplanner: Imperative path planning. In *Robotics: Science and Systems (RSS)*, 2023.

[47] R. Wang, Z. Hua, G. Liu, J. Zhang, J. Yan, F. Qi, S. Yang, J. Zhou, and X. Yang. A bi-level framework for learning to solve combinatorial optimization on graphs. *Advances in Neural Information Processing Systems*, 34:21453–21466, 2021.

[48] D. Nistér. An efficient solution to the five-point relative pose problem. *IEEE transactions on pattern analysis and machine intelligence*, 26(6):756–770, 2004.

[49] S. Khamis, S. Fanello, C. Rhemann, A. Kowdle, J. Valentin, and S. Izadi. Stereonet: Guided hierarchical refinement for real-time edge-aware depth prediction. In *Proceedings of the European Conference on Computer Vision (ECCV)*, pages 573–590, 2018.

[50] D. Sun, X. Yang, M.-Y. Liu, and J. Kautz. Pwc-net: Cnns for optical flow using pyramid, warping, and cost volume. In *Proceedings of the IEEE conference on computer vision and pattern recognition*, pages 8934–8943, 2018.

[51] J. Canny. A computational approach to edge detection. *IEEE Transactions on pattern analysis and machine intelligence*, 8(6):679–698, 1986.

[52] P. Wei, G. Hua, W. Huang, F. Meng, and H. Liu. Unsupervised monocular visual-inertial odometry network. In *Proceedings of the Twenty-Ninth International Conference on International Joint Conferences on Artificial Intelligence*, pages 2347–2354, 2021.

[53] M. Yang, Y. Chen, and H.-S. Kim. Efficient deep visual and inertial odometry with adaptive visual modality selection. In *Computer Vision–ECCV 2022: 17th European Conference, Tel Aviv, Israel, October 23–27, 2022, Proceedings, Part XXXVIII*, pages 233–250. Springer, 2022.

[54] L. Han, Y. Lin, G. Du, and S. Lian. Deepvio: Self-supervised deep learning of monocular visual inertial odometry using 3d geometric constraints. In *2019 IEEE/RSJ International Conference on Intelligent Robots and Systems (IROS)*, pages 6906–6913. IEEE, 2019.

[55] A. Geiger, P. Lenz, C. Stiller, and R. Urtasun. Vision meets robotics: The kitti dataset. *The International Journal of Robotics Research*, 32(11):1231–1237, 2013.

[56] M. Burri, J. Nikolic, P. Gohl, T. Schneider, J. Rehder, S. Omari, M. W. Achtelik, and R. Siegwart. The euroc micro aerial vehicle datasets. *The International Journal of Robotics Research*, 35(10):1157–1163, 2016.

[57] J. Sturm, N. Engelhard, F. Endres, W. Burgard, and D. Cremers. A benchmark for the evaluation of rgb-d slam systems. In *2012 IEEE/RSJ international conference on intelligent robots and systems*, pages 573–580. IEEE, 2012.

[58] Z. Teed and J. Deng. Deepv2d: Video to depth with differentiable structure from motion. *arXiv preprint arXiv:1812.04605*, 2018.

Appendix

A Closed-form Solutions to Scale Correction

As described in Section 3.2.1, the problem of scale estimation is formulated as a least squares optimization task aimed at minimizing the reprojection error over all pixels. Denoting the unknown true scale as s , the reprojection error at pixel (u, v) is

$$\mathcal{E}^{u,v} = K \left(d^{u,v} \mathbf{v} R_k^{k+1} K^{-1} \begin{bmatrix} u \\ v \\ 1 \end{bmatrix} + s \cdot \tau_k^{k+1} \right) - \lambda \begin{bmatrix} u + F_x^{u,v} \\ v + F_y^{u,v} \\ 1 \end{bmatrix}, \quad (6)$$

where K is the camera intrinsic matrix, $d^{u,v}$ is the depth at (u, v) , $\mathbf{v} R_k^{k+1}$ is the relative rotation, τ_k^{k+1} is the normalized translation direction, and $F_x^{u,v}, F_y^{u,v}$ are the horizontal and vertical optical flow at (u, v) . The dense depth is estimated by a disparity network [49], the optical flow is estimated by a flow network [50], and $\mathbf{v} R_k^{k+1}, \tau_k^{k+1}$ are estimated by a monocular VO backbone [9].

We then solve the least squares problem in (2) to get the optimal scale s^* . For efficiency, we proceed by reformulating it as a linear system and then utilize a closed-form solution to calculate s^* . Specifically, we first simplify the reprojection error in (6) by defining two auxiliary symbols

$$\alpha = \begin{bmatrix} \alpha_1 \\ \alpha_2 \\ \alpha_3 \end{bmatrix} = K \tau_k^{k+1}, \quad \beta = \begin{bmatrix} \beta_1 \\ \beta_2 \\ \beta_3 \end{bmatrix} = d^{u,v} K (\mathbf{v} R_k^{k+1}) K^{-1} \begin{bmatrix} u \\ v \\ 1 \end{bmatrix}. \quad (7)$$

Then, let $\mathcal{E}^{u,v} = 0$. By simplifying and combining terms, we obtain two equations in which all terms containing the variable s are situated on the left-hand side:

$$(\alpha_3 (u + F_x^{u,v}) - \alpha_1) s = \beta_1 - \beta_3 (u + F_x^{u,v}), \quad (8a)$$

$$(\alpha_3 (v + F_y^{u,v}) - \alpha_2) s = \beta_2 - \beta_3 (v + F_y^{u,v}). \quad (8b)$$

We can obtain two such constraints per pixel. In order to minimize the reprojection error, the optimal scale must comply with the constraints of all pixels to the greatest extent. We collectively comprise all the constraints together as a linear system:

$$Gs = \eta, \quad (9)$$

where G is the aggregated coefficients ahead s , η is the compounding values on the right-hand side. In practice, the images are preprocessed into a smaller size and some inefficient pixels are filtered out (described in Section 3.2.1), so the dimension of the linear system won't be too large. We then utilize the least squares solution to determine the optimal s^* efficiently,

$$s^* = (G^T G^{-1}) G^T \eta, \quad (10)$$

and finally, recover the translation with the estimated scale,

$$\mathbf{v} t_k^{k+1} = s^* \cdot \tau_k^{k+1}. \quad (11)$$